

Grain growth in U–7Mo alloy: A combined first-principles and phase field study



Zhi-Gang Mei*, Linyun Liang, Yeon Soo Kim, Tom Wiencek, Edward O'Hare, Abdellatif M. Yacout, Gerard Hofman, Mihai Anitescu

Argonne National Laboratory, 9700 South Cass Avenue, Argonne, IL 60439, USA

ARTICLE INFO

Article history:

Received 16 July 2015

Received in revised form

25 January 2016

Accepted 28 January 2016

Available online 1 February 2016

ABSTRACT

Grain size is an important factor in controlling the swelling behavior in irradiated U–Mo dispersion fuels. Increasing the grain size in U–Mo fuel particles by heat treatment is believed to delay the fuel swelling at high fission density. In this work, a multiscale simulation approach combining first-principles calculation and phase field modeling is used to investigate the grain growth behavior in U–7Mo alloy. The density functional theory based first-principles calculations were used to predict the material properties of U–7Mo alloy. The obtained grain boundary energies were then adopted as an input parameter for mesoscale phase field simulations. The effects of annealing temperature, annealing time and initial grain structures of fuel particles on the grain growth in U–7Mo alloy were examined. The predicted grain growth rate compares well with the empirical correlation derived from experiments.

© 2016 Elsevier B.V. All rights reserved.

1. Introduction

U–Mo alloys are among the most promising fuels for the future high performance research and test reactors due to its high uranium loading density and stable irradiation behavior [1]. Fission-induced swelling in U–Mo fuels is generally stable and predictable. A major contribution to the swelling comes from the yield of fission gases. Because of the extremely low solubility, fission gas atoms exist either in host lattice sites, or inside gas bubbles. In research reactors the operation temperature is usually low (<200 °C). Therefore, the formation and growth of fission gas bubbles are attributed mainly to the fission-enhanced diffusion [2]. At low burnups, fuel swelling by forming fission gas bubbles shows a stable linear dependence of fission density. Because of the high burnups pursued in U–Mo fuels, a phenomenon called recrystallization or grain subdivision takes place, which expedites the formation and growth of gas bubbles. Acceleration in fuel swelling at high burnups is closely related to this phenomenon. Recrystallization has been found to start at existing grain boundaries [3,4]. Hence increasing the grain size and reducing the grain boundary area by the thermal treatment of U–Mo alloy can effectively delay the recrystallization [5]. In addition to increasing the grain size, heating at high temperature is expected to anneal the defects

introduced during powder production, further delaying the recrystallization.

Several heat treatment approaches have been used for atomized U–Mo alloy powders. In the late 1990s, the performance of heat-treated U–10 wt.% Mo (simplified as U–10Mo, and similarly for U–7Mo) powders was investigated in the RERT-3 test irradiated in the ATR [6]. The atomized powders were heat treated at 800 °C for 100 h before hot-rolling of fuel plates. The temperature was selected to preserve the γ -phase of U–10Mo alloy. Considerable grain growth was observed after the heat treatment. Recently, Kim et al. heat treated atomized U–7Mo at 1000 °C for an hour in a vacuum furnace in order to apply a uranium nitride (UN) coating layer [5], in which the UN coating was applied to prevent the interaction between U–7Mo fuel particle and Al matrix. After heating, the grain size in U–7Mo powders increases from 6 μm to about 20 μm . Recently we also treated U–7Mo powders at 900 °C for one hour in quartz glass [7]. The grain size after heat treatment was found to be in the range of 10 μm and 30 μm . In order to obtain the desired grain size and grain size distribution, more heat treatment experiments should be conducted with different annealing time and temperatures, which are important for understanding the growth kinetics of the U–Mo alloys.

Mesoscale simulation methods, such as the phase field modeling, have been extensively used to study the temporal and spatial evolution of microstructures in various materials [8,9]. The kinetic and topological behaviors of grain growth in polycrystalline

* Corresponding author.

E-mail address: zmei@anl.gov (Z.-G. Mei).

materials can be well predicted by phase field methods, which also compare well with analytical models. Because of the scarcity of the fundamental thermophysical properties of U–Mo alloys, few phase field studies of the microstructure evolution in U–Mo alloys have been conducted, and most of them have relied on unphysical parameters.

The γ -phase of the U–Mo alloy used as nuclear fuel for research reactors is a solid solution system with a body-centered cubic (bcc) structure, which is stable only in the high temperature region. One of the common difficulties in atomistic simulation of solid solution systems is to mimic the random structure in a finite supercell. In first-principles calculations for solid solution systems, several approximations are used, such as the virtual crystal approximation (VCA) method proposed by Bellaiche and Vanderbilt [10]. In VCA, pseudopotentials are generated as the weighted average of the pseudopotential for each atomic species. However, the method is not suitable for alloys containing atoms of vastly different sizes. Recently, the special quasirandom structure (SQS) model proposed by Zunger et al. [11] has gained more popularity for analyzing the properties of solid solution systems. In this model, the randomness of atom distribution is introduced by emulating the correlation functions of an infinite random alloy within a finite supercell. The SQS models have been successfully applied to a number of alloy systems, such as U–Zr [12] and U–Mo [13]. For the phase field simulation of grain growth, the most important input parameters are the grain boundary properties, such as grain boundary energy and grain boundary mobility. To the best of our knowledge, no density functional theory (DFT) or molecular dynamics study of the grain boundary properties in γ U–Mo alloy have been carried out.

To this end, we investigated the grain growth in the γ U–7Mo alloy using a combined first-principles and phase field simulation approach. DFT-based first-principles calculations were utilized to predict the fundamental material properties of U–7Mo alloy. Using the predicted properties and applying the phase field method, we studied the effects of annealing temperature, annealing time and initial grain structure on the grain growth in U–7Mo alloy. The obtained grain growth rate was compared with the empirical correlation derived from experiment.

In Section 2, we discuss the methodology and computational details of the DFT calculations and phase field modeling. In Section 3 the results are presented and compared with experimental data. A summary of this work is given in Section 4.

2. Computational methodology

We first describe the computational details of DFT calculations and then discuss the formulation of the phase field model.

2.1. DFT calculations

In this study, the atomic structures of U–Mo alloys were modeled by the SQS method using the Alloy Theoretic Automated Toolkit (ATAT) code [14,15]. The SQS models of the bulk U–Mo alloy phase were constructed from a $4 \times 4 \times 4$ bcc supercell with 128 atoms. As an example, Fig. 1 shows the atomic structure of U–7Mo alloy using SQS. To perform DFT calculations, we used the projector augmented wave method (PAW) [16] as implemented in the Vienna *ab initio* simulation package (VASP) [17,18]. The exchange–correlation functional was described by the generalized gradient approximation (GGA) parameterized by Perdew Burke and Ernzerhof [19]. The $6s^2 6p^6 5f^2 7s^2$ and $4s^2 4p^6 4d^5 5s^1$ electrons were treated as valence electrons for U and Mo, respectively. The crystal structures were fully relaxed with respect to cell shape, cell volume, and atomic positions. In all cases the convergence criteria for the total energy and forces were set to 10^{-7} eV/atom and 10^{-2} eV/Å.

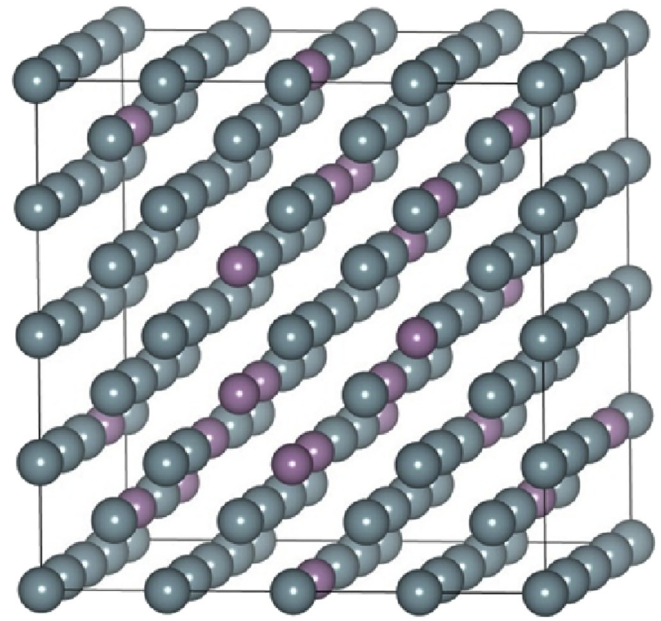


Fig. 1. SQS model of U–7Mo alloy with 128 atoms.

During the total energy calculations, the cut-off energy for the plane-wave expansion was set as 400 eV. Brillouin zone integrations were performed by using a set of $2 \times 2 \times 2$ k -points. Tests were made by using $3 \times 3 \times 3$ k -points in the case of U–7Mo as an example, and the final errors of the total energy difference were found to be less than 10^{-3} eV.

Two symmetric tilt grain boundaries (STGBs), $\Sigma 3(111)[110]$ and $\Sigma 5(310)[001]$, were studied in this work; these are frequently observed in bcc metal systems [20]. The standard method was used to construct the coincidence site lattice grain boundaries. The atomic structures for the STGBs were generated by GBstudio [21]. For the $\Sigma 3(111)$ GB, one grain of the bcc metal was rotated against the other grain around the common $[110]$ axis by about 70.53° , and the (111) plane was set as the GB plane. The $\Sigma 3(111)[110]$ GB was constructed by using an orthorhombic supercell with 48 atoms as shown in Fig. 2 (a). The unit vectors of the 48-atom based orthorhombic cell are $(1, 1, 2)a_0$, $(1, 1, 0)a_0$, and $(4, 4, 4)a_0$, with a_0 the lattice constant of the bcc metal, such as Mo. Similarly, $\Sigma 5(310)[001]$ GB was constructed by rotating one grain by about 36.9° , and the (310) plane is set as the GB plane. The $\Sigma 5(310)$ GB was constructed by using an orthorhombic supercell with 40 atoms as shown in Fig. 2 (b), with the unit vectors of the supercell as $(-1, 3, 0)a_0$, $(0, 0, 1)a_0$, and $(6, 2, 0)a_0$. The $\Sigma 3(111)[110]$ and $\Sigma 5(310)[001]$ GBs for the U–7Mo alloy system were created by applying the SQS model to the GB structures generated for the pure metal system, as shown in Fig. 3. Brillouin zone integrations were performed by using k -point meshes of $7 \times 12 \times 3$ and $5 \times 8 \times 3$ for the supercells of the $\Sigma 3(111)[110]$ and $\Sigma 5(310)[001]$ GBs, respectively. Other settings for the DFT calculations are similar to those for the bulk phases.

2.2. Phase field model formulation

In the phase field model, a large number of phase field variables $\eta_i(r)$ were used to distinguish the different orientations of grains, where the subscript i represents the number of grains. These variables are continuous functions of spatial coordinates and time. Within the grain i , the absolute value for η_i is one, while all other η_j ($j \neq i$) is zero. The value of η_i varies continuously from one to zero across the grain boundary. The total free energy of the interested

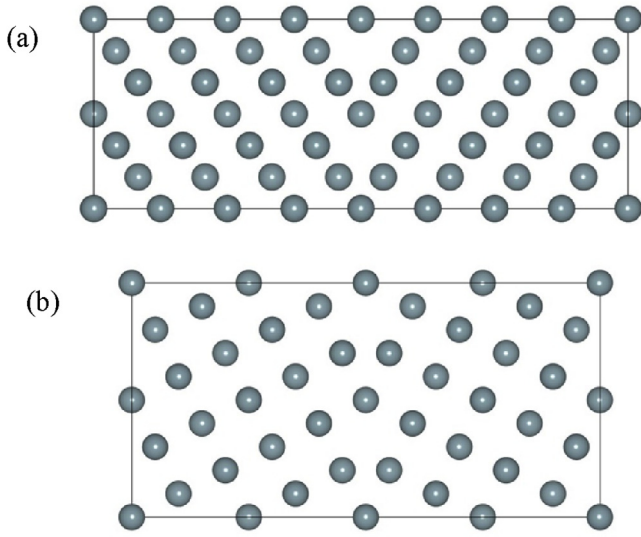


Fig. 2. Atomic structures of (a) $\Sigma 3(111)[110]$ and (b) $\Sigma 5(310)[001]$ STGBs for bcc metals, such as, Mo and U.

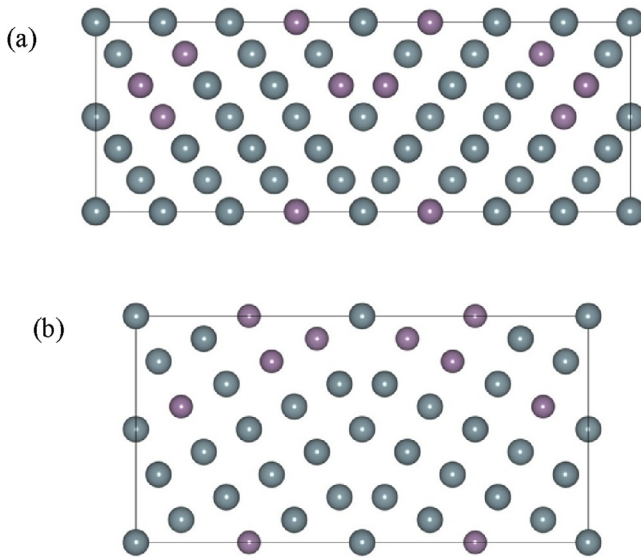


Fig. 3. Atomic structures of (a) $\Sigma 3(111)[110]$ and (b) $\Sigma 5(310)[001]$ STGBs for γ U–7Mo alloy. Blue and purple atoms represent the U and Mo atoms, respectively. (For interpretation of the references to colour in this figure legend, the reader is referred to the web version of this article.)

system can be represented in a Ginsburg-Landau form as [22,23]

$$F = \int \left[f_0(\eta_1, \eta_2, \dots, \eta_q) + \frac{1}{2} \kappa \sum_i \nabla^2 \eta_i(r) \right] d^3r, \quad (1)$$

where f_0 is the local free energy density of the system, the second term is the gradient energy term and κ is its gradient coefficient.

For modeling the grain growth in a pure system, the local free energy density function is constructed as [22,23]

$$f_0(\eta_1, \eta_2, \dots, \eta_q) = \sum_{i=1}^q \left(-\frac{A}{2} \eta_i^2 + \frac{B}{4} \eta_i^4 \right) + C \sum_{i=1}^q \sum_{j \neq i}^q \eta_i^2 \eta_j^2 + \frac{1}{4}, \quad (2)$$

where A , B , and C are positive constants, and q represents the total number of grain orientations in a grain structure. If we integrate the free energy, it is entirely related to the grain boundary properties. Thus, the expansion coefficients of the free energy can be determined from the grain boundary properties of U–7Mo alloys [24].

The spatial and temporal evolutions of grain parameters follow the Allen-Cahn equation [9],

$$\frac{\partial \eta_i}{\partial t} = -L \frac{\delta F}{\delta \eta_i}, \quad i = 1, 2, \dots, q. \quad (3)$$

where L is the kinetic coefficient of grain boundary movement.

To take into account the spherical shape of the U–7Mo alloy particle, we introduce a domain parameter to distinguish the U–7Mo particle and the Al matrix as shown in Fig. 4. A domain parameter ϕ is introduced to describe the U–7Mo phase with $\phi = 1$ and the Al matrix phase with $\phi = 0$ as depicted in the figure, where ϕ is a continuous variable and smoothly change from 0 to 1 across the interface between the U–7Mo particle and Al matrix. Since the particle is fixed in our simulation, ϕ does not evolve with time. The kinetic coefficient L_0 depends on the domain parameter as [25], $L_0(\phi) = L_\alpha h(\phi) + L_\beta (1 - h(\phi))$. Here L_α is the kinetic coefficient for the U–7Mo particle, and L_β is a very small value to ensure that no grain boundary movement occurs outside the U–7Mo particle, and $h(\phi)$ is an interpolation function having the form $h(\phi) = \phi^3(6\phi^2 - 15\phi + 10)$, which is plotted in Fig. 4(b).

The temperature effect can be considered in the kinetic coefficient L according to the Arrhenius formula as [26]

$$L(\phi) = L_0(\phi) e^{-\frac{Q}{k_B T}}, \quad (4)$$

where k_B is the Boltzmann's constant, T is the temperature, and Q is the activation energy of grain boundary diffusion.

In order to quantitatively simulate the U–7Mo alloy based on this model, the grain boundary energy, grain boundary mobility, and activation energy have to be determined by atomic calculations or experiments. In this work, the grain boundary energy is predicted by DFT method as outline earlier. Based on this information, the expansion coefficients of chemical free energy and the gradient coefficients can be determined. Due to the difficulty of calculating the grain boundary mobility, this value will be calibrated based on the experimental measurement of grain size with different annealing times. The details of deriving these parameters are provided in Sec. 3.

The phase field model was implemented in an in-house simulation code and the semi-implicit FFTW numerical method was employed to solve the Allen-Cahn equations [27]. Periodic boundary conditions were imposed on the simulation domain. The time step for the evolution was $t = 3.0$ s, and the spacing was $\Delta x = \Delta y = 1.0 \mu\text{m}$. A model size of $200 \mu\text{m} \times 200 \mu\text{m}$ and a U–7Mo circular plate size of $180 \mu\text{m}$ were used in the simulations.

3. Results and discussion

We discuss in this section the materials properties and grain growth results from the DFT and phase field modeling studies, respectively.

3.1. Material properties of U–Mo alloys by DFT

Consistent with previous investigations of U metal, our study shows that the bcc γ -phase of U is stable only at high temperature. The calculated total energy of the γ -U phase is about 0.27 eV/atom higher than that of the low-temperature α -U phase. Elements, such as Mo and Zr, are therefore used to stabilize the γ -U phase to lower

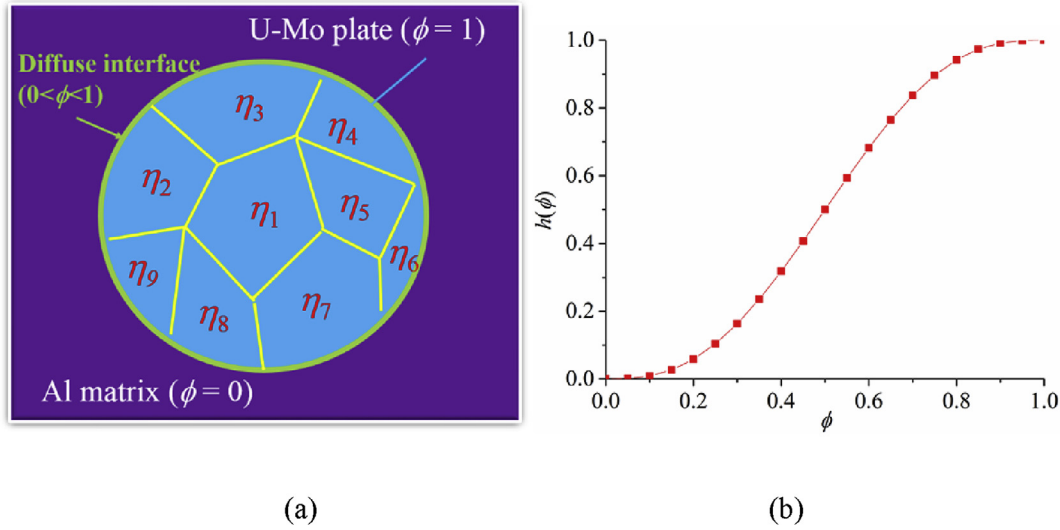


Fig. 4. (a) Schematic diagram of a U–7Mo fuel particle with multiple grains embedded in the Al matrix. (b) Plot of h function vs domain parameter.

temperature. To evaluate the thermodynamic stability of the γ U–Mo alloy, we estimated the enthalpy of formation of the γ U–Mo alloy phase. With bcc Mo and γ -U as the reference states for elements Mo and U, the calculated enthalpy of formation shows that γ U–7Mo alloy is thermodynamically stable at high temperature above 600 °C while it is unstable at room temperature with respect to bcc Mo and α -U (more details will be presented elsewhere). Therefore the γ U–7Mo phase observed at room temperature is a metastable phase.

To further examine the mechanical stability of the γ U–Mo alloys, we investigated the elastic properties of the γ U–7Mo phase. Single-crystal elastic constants of a solid phase can be calculated by the stress-strain method [28]. In this work, the single-crystal elastic constants are determined based on the applied strains of ± 0.01 . From the predicted elastic constants, the polycrystalline properties including bulk modulus (B), shear modulus (G), Young's modulus (E) and Poisson's ration (ν) can be determined by the Voight-Reuss-Hill approach [29]. Table 1 summarizes the predicted single-crystal elastic constants and polycrystalline properties of bcc Mo, γ -U and U–7Mo phases. In these three systems, only bcc Mo has been previously measured for its elastic properties. The currently predicted elastic constants and polycrystalline moduli of bcc Mo agree perfectly with the experimental data by Dickinson and Armstrong [30], with an average error less than 2%. In comparison with bcc Mo, the predicted elastic constants of γ -U are considerable smaller, especially the bulk modulus, indicating its weaker bonding than that in bcc Mo.

The shear constant $C' = (C_{11} - C_{12})/2$ of γ -U is predicted to be negative, as shown in Table 1. The negative shear constant of the γ -U phase indicates its mechanical instability, which is in agreement with the previous study by Beeler et al. [31]. So far, because of the

unstable nature at room temperature, no experimental or theoretical study of the elastic properties of γ U–Mo alloys has been reported. Predicting the elastic properties of alloy phases by DFT is theoretically challenging. The SQS method in general breaks the point group symmetry. The configurational disorder usually results in a triclinic lattice for a finite supercell. For the bcc γ U–Mo alloy phases, the SQS approach results in elastic tensors with 21 nonvanishing elements. Theoretically, there should be only three independent elastic constants C_{11} , C_{12} , and C_{44} for cubic systems. According to Tasnadi et al. [32], the closest cubic elastic constants can be obtained by simple averaging,

$$\bar{C}_{11} = \frac{C_{11} + C_{22} + C_{33}}{3}, \quad \bar{C}_{12} = \frac{C_{12} + C_{13} + C_{23}}{3}, \quad \text{and} \quad \bar{C}_{44} = \frac{C_{44} + C_{55} + C_{66}}{3}. \quad (5)$$

The cubic-averaged elastic constants of the γ U–7Mo alloy together with its polycrystalline properties are shown in Table 1. Upon alloying Mo in γ -U, the shear constant C' of γ U–7Mo alloy becomes positive, indicating that the isotropic γ phase of U can be mechanically stabilized by alloying Mo.

Based on the studies of the bulk phase, we further investigated the grain boundary properties in γ U–Mo alloys. In this work, we focus on only two representative STGBs in the bcc γ U–7Mo alloy: $\Sigma 3(111)[110]$ and $\Sigma 5(310)[001]$ GBs. We define the grain boundary energy (γ_{GB}) as

$$\gamma_{GB} = \frac{E_{GB} - E_{SC}}{2A}, \quad (6)$$

where E_{GB} and E_{SC} are the total energies of the GB supercell and its corresponding single crystal, respectively. The latter is obtained by the bulk supercell with periodicity similar to that of the GB supercell. A is the area of the GB plane, and the expression is divided by 2 because of the two interfaces in the supercell. For completeness, we also study the GBs of bcc Mo and γ -U. Fig. 2 shows the created atomic structures of the $\Sigma 3(111)[110]$ and $\Sigma 5(310)[001]$ GBs for pure metals Mo and U. The grain boundary energy of $\Sigma 3(111)[110]$ of bcc Mo is predicted to be 2.12 J/m², while the formation energy of $\Sigma 5(310)[001]$ is predicted to be 1.78 J/m², as shown in Table 2. The grain boundary properties of Mo were previously studied by DFT, and two values were reported for the

Table 1

Calculated elastic properties of bcc Mo, γ -U and γ U–7Mo, including elastic constants C_{ij} (GPa), shear constant (GPa), bulk modulus (GPa), shear modulus (GPa), Young's modulus (GPa), and Poisson ratio.

	C_{11}	C_{12}	C_{44}	C'	B	G	E	ν	Reference
Bcc Mo	466	157	103	155	260	122	316	0.298	This work
	464	158	109	153	260	125	323	0.293	Expt. [30]
γ -U	94	154	34	−30	134	114	225	0.169	This work
	86	155	37	−35	132	113	265	0.17	Calc. [31]
U–7Mo	173	138	50	23	143	36	100	0.383	This work

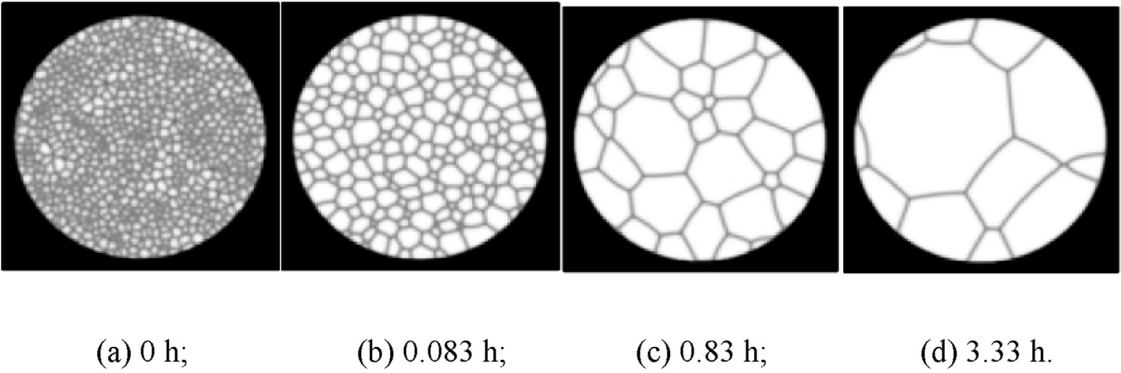
Table 2
Grain boundary energy (eV) in bcc Mo, γ -U and γ U–7Mo calculated by DFT.

	$\Sigma 3(111)[110]$	$\Sigma 5(310)[100]$	Reference
Bcc Mo	2.12	1.78	This work
		1.70 [20], 1.52 [33]	Calc.
γ -U	0.13	0.52	This work
U–7Mo	0.37	0.63	This work

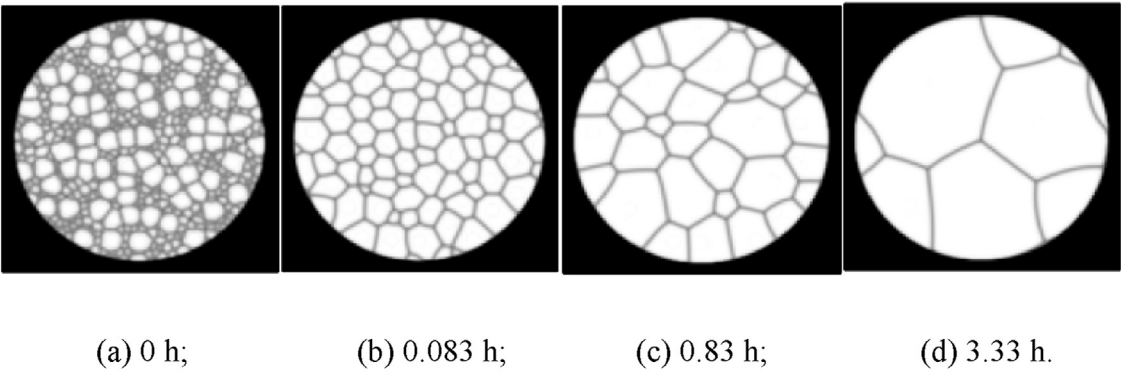
Table 3
U–Mo powder annealing test results from previous experimental studies.

	Temperature (°C)	Time (s)	Grain size (μm)
ANL RERTR-3 [6]	800	360000	22
ANL [7]	900	3600	23
KAERI [41]	1000	3600	20
ANL [7]	1000	1800	24

Case I:



Case II:



Case III:

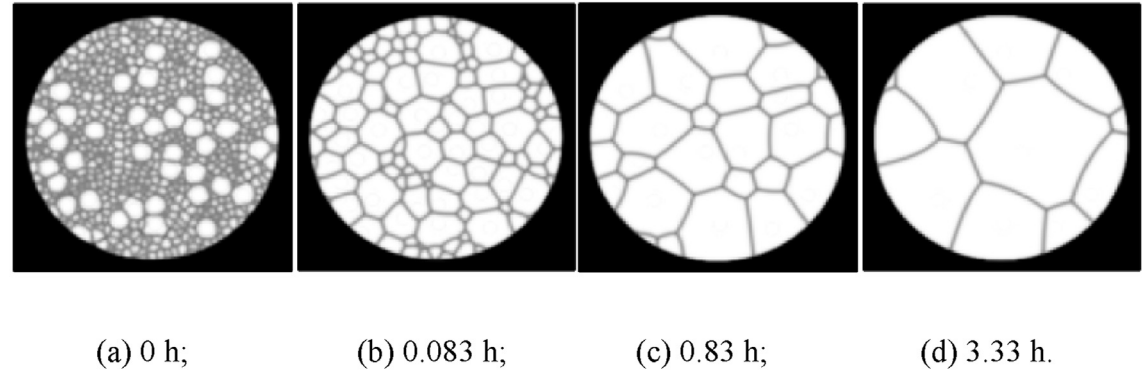


Fig. 5. Temporal evolution of the grain structures in a U–7Mo particle at 1000 °C: (a) 0 h; (b) 0.083 h; (c) 0.83 h; and (d) 3.33 h. Case I: The initial grain size in the fuel particle is 100% 3 μm . Case II: The initial grain size in the fuel particle is 50% 3 μm and 50% 15 μm . Case III: The initial grain size in the fuel particle is 75% 3 μm and 25% 15 μm .

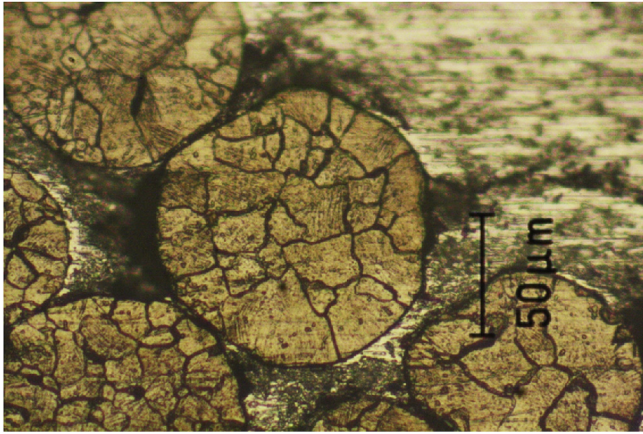


Fig. 6. Optical micrograph image of ZrN coated U–7Mo fuel particles embedded in Al matrix after heat treatment at 1000 °C for half an hour.

$\Sigma 5(310)$ boundary, 1.80 [20] and 1.55 J/m² [33], which are close to our results. The grain boundary energies in Mo have also been extensively studied by molecular dynamics simulations [34]. However, these energies are usually lower than those computed by DFT. Because of the mechanical unstable character of the γ -U phase, studying the GB properties is not straightforward. Without constraint, the GB structure of γ -U can be destroyed in the structural relaxation, and unrealistic negative GB formation energies will be predicted. Therefore only the first few layers of atoms close to grain boundaries were allowed to relax. In this work, the grain boundary energies for $\Sigma 3(111)[110]$ and $\Sigma 5(310)[001]$ GBs in γ -U are predicted to be 0.13 and 0.52 J/m², respectively. We noticed that the grain boundary energies of γ -U are much lower than those of bcc Mo, indicating a weaker bonding in γ -U than those in bcc Mo. To construct the GBs for the U–Mo alloy phase, we applied the SQS models to the GBs created for bcc metals. Fig. 3 shows the created $\Sigma 3(111)[110]$ and $\Sigma 5(310)[001]$ GBs for γ U–7Mo. The grain boundary energies in the γ U–7Mo alloy are predicted to be 0.37 J/m² and 0.63 J/m², for $\Sigma 3(111)[110]$ and $\Sigma 5(310)[001]$ GBs, respectively. The grain boundary energies in the U–Mo alloy lie between those of pure γ U and bcc Mo, which is consistent with the

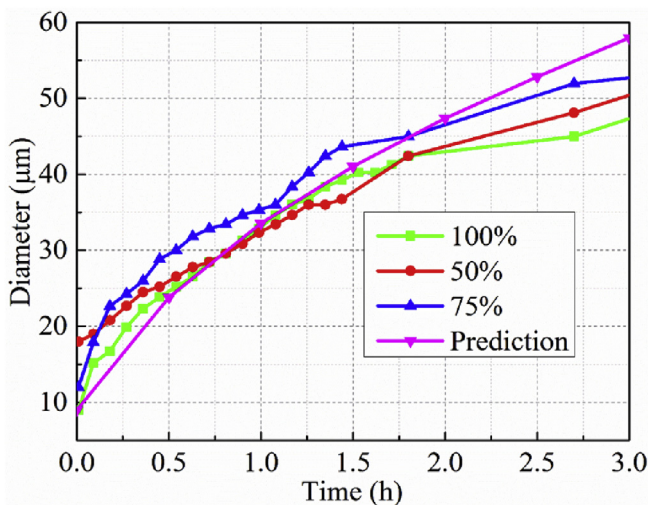


Fig. 7. Average grain size in a U–7Mo particle vs time at 1000 °C with an initial grain structure having 100% 3 μm sized grains, 50% 3 μm and 50% 15 μm sized grains, and 75% 3 μm and 25% 15 μm sized grains, respectively. The experimentally predicted grain size is also plotted.

predicted elastic properties of these systems.

3.2. Grain growth in U–7Mo alloy by phase field modeling

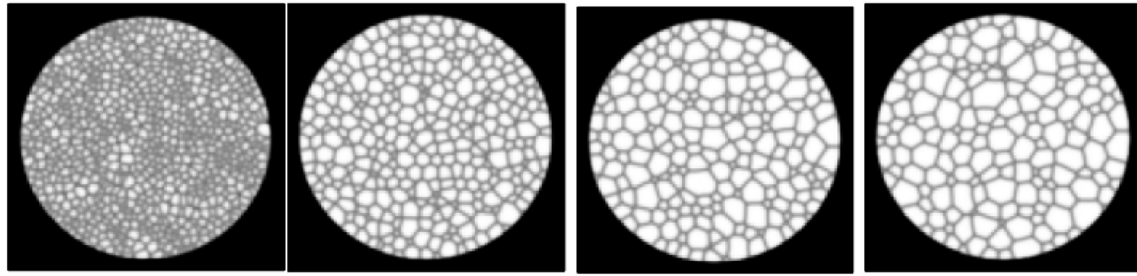
Reliable physical parameters are critical to a quantitative phase field modeling of grain growth of U–7Mo alloy. However, due to the scarcity of experimental studies of U–7Mo alloy, most of these data are not available yet. Therefore, we rely on atomistic simulation methods, such as first-principles methods, to provide such information. We investigated several fundamental thermophysical properties of U–7Mo alloy using first-principles method for the first time. The predicted grain boundary energy was utilized to derive the gradient coefficient and the coefficients for the free energy function. Although other properties, such as elastic constants, are not directly used in the current phase field modeling of grain growth, they may be used to study the stress effect on the grain growth in the future.

In real polycrystalline U–7Mo alloy samples, the grain boundary energy σ_{gb} and mobility M vary from grain boundary to grain boundary, depending on the grain boundary misorientation and inclination. However, the mathematical models usually ignore the variation of grain boundary energy and mobility. In the present simulations a single value for σ_{gb} and M was used for all grain boundaries. This simplified scenario, which is called idea grain growth [35–38], is used extensively by computer simulation.

The input parameters for the phase field simulations are determined as follows. With the grain boundary energies of $\Sigma 3(111)[110]$ and $\Sigma 5(310)[001]$ GBs determined from the DFT calculations in Sec. 3.1, we adopted the relatively smaller value of $\sigma_{gb} = 0.37$ J/m² ($\Sigma 3(111)[110]$ GB) in our phase field simulations, which may correspond to the most stable grain structure. The thickness used in the simulation is assumed to be 4.0×10^{-6} m, which is approximately four grid points at the grain boundary region. According to the relationships $\sigma = \sqrt{2A\kappa}/3$ and $l = \sqrt{8\kappa/A}$ derived by Moelans et al. [24] for a symmetrical phase parameter profile with the saddle point of the energy density located at $\eta_i = 0.5$, the gradient coefficient κ and coefficient A of the free energy function are determined to be 1.11×10^{-6} J/m and 5.55×10^5 J/m³, respectively. Accordingly, the other two free energy coefficients B and C are determined to be 5.55×10^5 J/m³ and 8.33×10^5 J/m³, respectively. The activation energy for the GB diffusion of U–7Mo is unavailable in the literature, to our best knowledge. Therefore, for the work reported here, we adopted the activation energy of the GB diffusion measured for Mo [39], that is 2.73 eV. We believe this value should be close to that for the U–7Mo alloy, because Mo is the element with much slower diffusivity in U–Mo alloys [40]. The kinetic coefficient L_0 is related to the GB mobility. Because of the difficulty of calculating this value, we use the experimental data to fit it. In experiments the grain size has been shown to increase from 3 μm to 24 μm after 0.5 h (see Table 3) at temperature 1000 °C [7]. Thus, we can derive L_0 based on the time required for the grain size to increase from 3 μm to 24 μm in the phase field simulation. L_0 is determined to be 1.04×10^{-7} m³/(Js). To give a diffuse interface profile of the domain parameter, we use the function $\phi = 0.5 - 0.5 \left(\tanh \frac{R-R_0}{\tau} \right)$, where $R_0 = 90$ μm is the radius of the U–7Mo particle, $\tau = 2.0$, and R measures the radius of any grid to the particle center.

In order to study the statistically averaged kinetics and topological features of the ideal two-dimensional grain growth in the phase field model, computer simulations are performed on a simple square lattice by solving Eq. (3). The initial condition of the grain structure in the simulation corresponds to the particle size of 3 μm, which is consistent with the experimental conditions. The temporal evolution of grain structures at different temperatures and with different initial grain size are studied in detail. In order to

Case I:



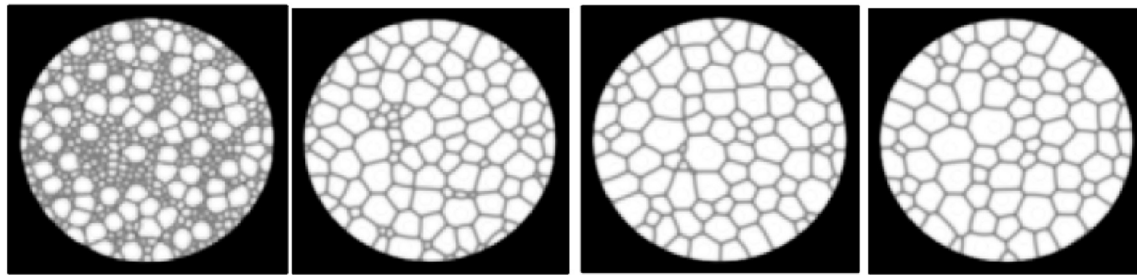
(a) 0 h;

(b) 4.1 h;

(c) 8.1 h;

(d) 10.5 h.

Case II.



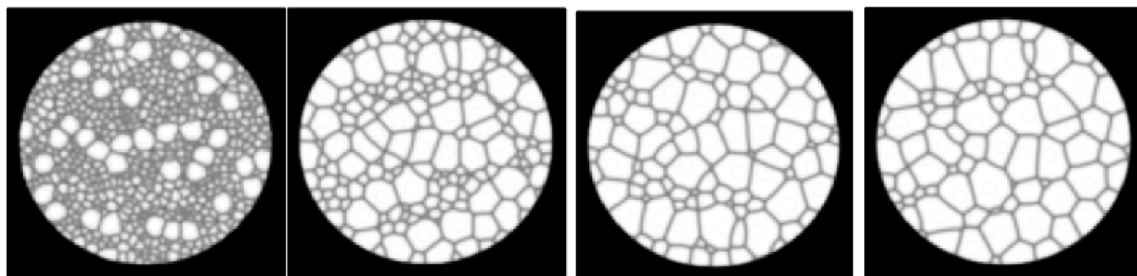
(a) 0 h;

(b) 4.1 h;

(c) 8.1 h;

(d) 10.5 h.

Case III.



(a) 0 h;

(b) 4.1 h;

(c) 8.1 h;

(d) 10.5 h.

Fig. 8. Temporal evolution of the grain structures in a U–7Mo particle at 900 °C: (a) 0 h; (b) 4.1 h; (c) 8.1 h; and (d) 10.5 h. Case I: The initial grain size in the fuel particle is 100% 3 μm . Case II: The initial grain size in the fuel particle is 50% 3 μm and 50% 15 μm . Case III: The initial grain size in the fuel particle is 75% 3 μm and 25% 15 μm .

differentiate the different grains in the simulations, a function $\xi(r) = \sum_{i=1}^p \eta_i^2(r)$ is used, which takes a value of unity within the individual grain and a smaller value along the grain boundary region. Fig. 5 shows the grain structures as a function of time with different initial structures heated at a temperature of 1000 °C. The bright regions are grain interiors and the dark lines are grain boundaries. Three different initial grain structures are tested as examples, as shown in Fig. 5: case I with 100% 3 μm sized grains, case II with 50% 3 μm and 50% 15 μm sized grains, and case II with 75% 3 μm and 25% 15 μm sized grains. Because of the high annealing temperature, grain boundaries move rapidly, and grains

grow in all three cases. The simulation results show that the grain growth is faster with a higher percentage of large grains in the initial structure of the fuel particle. As a comparison, Fig. 6 shows the typical optical micrograph of U–7Mo fuel particles embedded in an Al matrix that was heat treated at 1000 °C for half an hour [7]. We want to point out that the circular domain used for the fuel particle can affect the grain shapes at domain boundary. Because of the smooth function of mobility applied on the circular domain, the grain boundaries at the domain boundary do not move, and only the grain boundaries inside the particle evolve. Thus, the grains near the domain boundary evolve differently from the grains inside

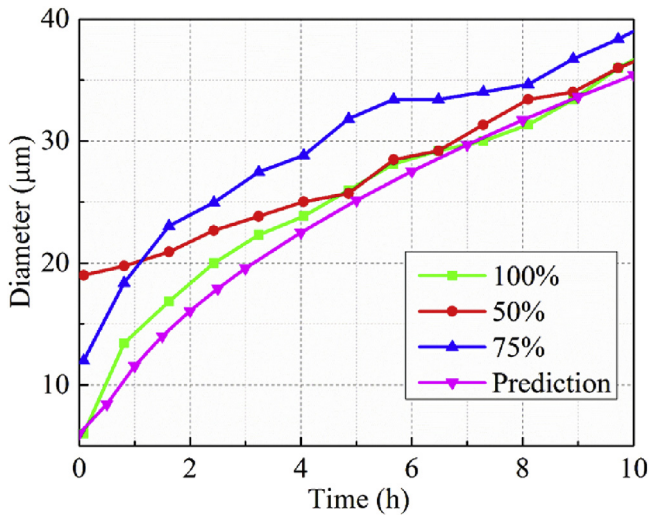


Fig. 9. Average grain size in a U–7Mo particle vs time at 900 °C with an initial grain structure having 100% 3 μm sized grains, 50% 3 μm and 50% 15 μm sized grains, and 75% 3 μm and 25% 15 μm sized grains, respectively. The experimentally predicted grain size is also plotted.

the particle, which may result in irregular grain shapes at the later stage.

Since the measured grain size data is limited, we have derived a correlation based on the experimental data [7,41] as shown in Table 3 in order to compare with the current simulation results. The correlation function relates the grain size with the heating time as $d^2 = d_0^2 + 4.63 \times 10^{10} \exp\left(-\frac{32752}{T}\right)t$, where d_0 is the average grain size in the as-fabricated fuel particles (in μm) and t is the time. The time dependence of the average grain size in the fuel particles with three different grain structures, together with the correlation derived from experimental data, is shown in Fig. 7. The average grain size in the particle is estimated by dividing the total area of the fuel particle by the total number of grains. Good agreement between the simulated results and the experimental estimation is obtained when the annealing time is less than 2 h. Beyond 2 h, however, a notable deviation appears. This is due to the small number of grains in the fuel particle at the late stage of annealing, which increases the uncertainty of the estimated grain size. Therefore, calculation of the grain size at the late stage largely depends on the configuration of the grain structure. We note that the system with initial 50% 3 μm and 50% 15 μm sized grains evolves faster than the one with 100% 3 μm sized grains. The reason is that a certain amount of large grains in the system can help the small grains grow faster in the early stage, which makes the average grain size increase faster than the case with 100% small grains. As shown in Fig. 5, the small grains in case II shrink noticeably faster than those in case I with 100% 3 μm grains. However, when the system has 75% 3 μm and 25% 15 μm sized grains as shown in case III, it evolves even faster than the one in case II with 50% 3 μm and 50% 15 μm sized grains. We believe this phenomenon is related to the grain distributions in the fuel particle. For case III with 25% large grains, when the large grains are distributed homogeneously in the structure (meaning that large grains are surrounded by abundant small grains), both the small and large grains can grow easily by consuming nearby small grains through the movement of grain boundaries and thus form larger grains. However, for case II with 50% large grains, the large grains have a high chance to be contacted with nearby large grains. It takes longer time to form larger grains by the movement of large grain boundaries than that by small grains. Therefore, the grain growth rate in case II with 50% large grains is lower than that of case III with 25% large grains. This result

indicates that adding a small amount of large grains in the initial particle can help increase the grain growth rate significantly.

To investigate the effect of temperature on grain growth, we also simulated the evolution of grain structure at a lower temperature of 900 °C. Fig. 8 plots the temporal evolutions of grain structures for three different initial grain size distributions. The time dependence of the average grain size in the fuel particles with three different grain structures, together with the correlation derived from experimental data, is shown in Fig. 9. The predicted growth rates agree well with the experimental results. The system with 75% 3 μm and 25% 15 μm sized grains shows the highest growth rate among the three cases. The case with initial 50% 3 μm and 50% 15 μm sized grains evolves faster than the 100% 3 μm grain case. The fact that the average grain size of the case with 50% 3 μm and 50% 15 μm initial grains is larger than the other two cases before 1 h is due to the initial large amount of large grains in the system. These results are consistent with the simulated results at 1000 °C.

Compared with the grain structures treated at 900 °C, the grain size in the fuel particle treated at 1000 °C is significantly larger. For example, the average grain size increases from 18 μm to 43 μm after 2 h when the temperature increased from 900 °C to 1000 °C. Therefore, the annealing time required for the desired grain size can be considerably reduced at higher temperature. The different initial grain size distribution also plays an important role in the grain growth rate. By including a small amount of large grain, the grain growth rate can be markedly enhanced for U–Mo fuel particles. However, it is worth noting that the grain growth rate is also affected by the distribution of large grains in the fuel particle. Therefore, it is difficult to quantify an optimal amount of large grains which leads to the largest grain growth rate.

4. Conclusions

Using a multiscale simulation approach, we investigated the grain growth in U–7Mo alloy for nuclear fuel applications. DFT calculations were used to study the mechanical stability of γ U–7Mo alloy based on the predicted elastic properties. Two grain boundaries, Σ3(111)[110] and Σ5(310)[001], were investigated for γ U–7Mo and compared with those of pure bcc Mo and U metals. Using the predicted grain boundary properties as input parameters, we studied the effects of annealing temperature, annealing time and initial grain structure on the grain growth in U–7Mo alloy particles by the phase field approach. Increasing the heating temperature is found to effectively reduce the annealing time required for the desired grain size. We found that the fuel particle with a certain amount of mixed sized grains has a faster grain growth rate than those with identical sized grains. The predicted grain growth rate is in good agreement with the empirical correlation derived from experimental measurements. We expect that the currently predicted kinetic model for the grain growth in the U–7Mo will be helpful in determining the optimal experimental conditions for annealing.

Acknowledgments

This work is sponsored by the U.S. Department of Energy, National Nuclear Security Administration (NNSA), Office of Material Management and Minimization (NA-23) Reactor Conversion Program. Use of the Center for Nanoscale Materials, an Office of Science user facility, was supported by the U. S. Department of Energy, Office of Science, Office of Basic Energy Sciences, under Contract No. DE-AC02-06CH11357. We gratefully acknowledge the computing resources provided on Blues, a high-performance computing cluster operated by the Laboratory Computing Resource Center at Argonne National Laboratory.

References

- [1] Y.S. Kim, G.L. Hofman, M.R. Finlay, J.L. Snelgrove, S.L. Hayes, M.K. Meyer, C.R. Clark, F. Huet, The 25th International Meeting on Reduced Enrichment for Research and Test Reactors, RERTR, Chicago, Illinois, 2003.
- [2] J. Rest, G.L. Hofman, Y.S. Kim, J. Nucl. Mater. 385 (2009) 563.
- [3] J. Rest, J. Nucl. Mater. 346 (2005) 226.
- [4] Y.S. Kim, G.L. Hofman, J.S. Cheon, J. Nucl. Mater. 436 (2013) 14.
- [5] Y.S. Kim, J.M. Park, K.H. Lee, B.O. Yoo, H.J. Ryu, B. Ye, J. Nucl. Mater. 454 (2014) 238.
- [6] J.M. Park, Y.S. Han, K.H. Kim, Y.S. Lee, C.K. Kim, Fabrication and characterization of atomized U-Mo powder dispersed fuel compacts for the RERTR-3 irradiation test, in: The 25th International Meeting on Reduced Enrichment for Research and Test Reactors (RERTR). Budapest, Hungary, 1999.
- [7] T.C. Wiencek, E. O'Hare. (2015) (unpublished work).
- [8] L.Q. Chen, Annu. Rev. Mater. Res. 32 (2002) 113.
- [9] I. Steinbach, Annu. Rev. Mater. Res. 43 (43) (2013) 89.
- [10] L. Bellaiche, D. Vanderbilt, Phys. Rev. B 61 (2000) 7877.
- [11] A. Zunger, S.H. Wei, L.G. Ferreira, J.E. Bernard, Phys. Rev. Lett. 65 (1990) 353.
- [12] A. Landa, P. Söderlind, P.E.A. Turchi, L. Vitos, A. Ruban, J. Nucl. Mater. 385 (2009) 68.
- [13] A. Landa, P. Söderlind, P.E.A. Turchi, J. Nucl. Mater. 414 (2011) 132.
- [14] A. van de Walle, G. Ceder, J. Phase Equilib. 23 (2002) 348.
- [15] A. van de Walle, P. Tiwary, M. de Jong, D.L. Olmsted, M. Asta, A. Dick, D. Shin, Y. Wang, L.Q. Chen, Z.K. Liu, Calphad 42 (2013) 13.
- [16] P.E. Blöchl, Phys. Rev. B 50 (1994) 17953.
- [17] G. Kresse, J. Furthmüller, Phys. Rev. B 54 (1996) 11169.
- [18] G. Kresse, D. Joubert, Phys. Rev. B 59 (1999) 1758.
- [19] J.P. Perdew, K. Burke, M. Ernzerhof, Phys. Rev. Lett. 77 (1996) 3865.
- [20] T. Ochs, C. Elsässer, M. Mrovec, V. Vitek, J. Belak, J.A. Moriarty, Philos. Mag. A 80 (2000) 2405.
- [21] H. Ogawa, Mater. Trans. 47 (2006) 2706.
- [22] D. Fan, L.Q. Chen, Acta Mater. 45 (1997) 611.
- [23] D.N. Fan, C.W. Geng, L.Q. Chen, Acta Mater. 45 (1997) 1115.
- [24] N. Moelans, B. Blanpain, P. Wollants, Phys. Rev. B 78 (2008).
- [25] L.Y. Liang, M. Stan, M. Anitescu, Appl. Phys. Lett. 105 (2014).
- [26] M. Wang, B.Y. Zong, G. Wang, Comput. Mater. Sci. 45 (2009) 217.
- [27] L.Q. Chen, J. Shen, Comput. Phys. Commun. 108 (1998) 147.
- [28] S. Shang, Y. Wang, Z.-K. Liu, Appl. Phys. Lett. 90 (2007) 101909.
- [29] D.H. Chung, W.R. Buessem, J. Appl. Phys. 38 (1967) 2535.
- [30] J.M. Dickinson, P.E. Armstrong, J. Appl. Phys. 38 (1967) 602.
- [31] B. Beeler, C. Deo, M. Baskes, M. Okuniewski, J. Nucl. Mater. 433 (2013) 143.
- [32] F. Tasnádi, M. Odén, I.A. Abrikosov, Phys. Rev. B 85 (2012) 144112.
- [33] A.M. Tahir, R. Janisch, A. Hartmaier, Model. Simul. Mater. Sci. Eng. 21 (2013) 075005.
- [34] S. Ratanaphan, D.L. Olmsted, V.V. Bulatov, E.A. Holm, A.D. Rollett, G.S. Rohrer, Acta Mater. 88 (2015) 346.
- [35] N. Moelans, F. Wendler, B. Nestler, Comput. Mater. Sci. 46 (2009) 479.
- [36] C.E. Krill, L.Q. Chen, Acta Mater. 50 (2002) 3057.
- [37] R.D. Kamachali, I. Steinbach, Acta Mater. 60 (2012) 2719.
- [38] S.G. Kim, D.I. Kim, W.T. Kim, Y.B. Park, Phys. Rev. E 74 (2006).
- [39] D.C. Blaine, J.D. Gurosik, S.J. Park, D.F. Heaney, R.M. German, Metall. Mater. Trans. A Phys. Metall. Mater. Sci. 37A (2006) 715.
- [40] D.E. Smirnova, A.Y. Kuksin, S.V. Starikov, J. Nucl. Mater. 458 (2015) 304.
- [41] J.M. Park. (2015) (unpublished work).